The Internal Tide off the West Coast of Vancouver Island

P. G. DRAKOPOULOS* AND R. F. MARSDEN

Department of Physics, Royal Roads Military College, Victoria, British Columbia, Canada

(Manuscript received 18 March 1991, in final form 22 June 1992)

ABSTRACT

Using data from the Coastal Ocean Dynamics Experiment (CODE) and the Island Coastal Current Experiment, the internal tide off the west coast of the Vancouver Island was studied. Although the semidiurnal barotropic velocity field in the area was weak, the baroclinic field was found to be relatively strong with speeds up to five times greater. The intermittent nature of the baroclinic field was resolved by estimating the M_2 tidal harmonic coefficients every 24 hours in 15-day overlaping intervals. These time-evolving coefficients were then analyzed using spectral analysis methods. For most of the area under investigation, the internal tide was generated mainly at the shelf break and was found to propagate cross-shore. Off Estevan point, where the bottom contour is regular, the beam structure was identified and traced to distances 40 km from the generation region on the slope. The downward-propagating beam was found to follow the seasonal variation of the characteristic propagation paths. An empirical orthogonal function analysis revealed a highly coherent baroclinic field (78% of the M_2 variance). The predictions of an internal tide model were found to be in good agreement with the experimental results on the slope. The interaction of a cyclonic eddy, present in the area during August 1980, with the internal tide was also addressed.

1. Introduction

From May 1979 to September 1980, a major current meter study was performed off the west coast of Vancouver Island known as the Coastal Ocean Dynamics Experiment (CODE). Results from tidal analyses performed on the data (e.g., Hugget et al. 1987), revealed strong diurnal (K_1) but weak semidiurnal (M_2) currents along the continental margin of Vancouver Island. Consequently, the bulk of the subsequent investigation, for example, Thomson and Crawford (1982) and Crawford and Thomson (1982), focused on the diurnal tide. However, recent numerical models of the area (Foreman and Walters 1990; and Flather 1988) suggested the presence of semidiurnal tidal energy in excess of that predicted by barotropic models. This energy has been attributed to the existence of internal waves with tidal frequency, also known as internal tides. The first attempt to detect such tides in the area was by Larsen et al. (1972) and later followed by Barbee (1975). Barbee was successful in measuring the internal tide field in a mooring located seaward of the continental shelf break off Tofino. However, his results did not compare well with a model by Prinsenberg and Rattray (1975). In this paper, the origin and the temporal and spatial variability of the baroclinic tidal currents were investigated using observations from the CODE experiment.

Internal tides are not the result of direct astronomical forcing but owe their existence to the interaction of the barotropic (surface) tide with the bottom topography (e.g., Wunsch 1975). For a sloping bottom, the barotropic tide can force the flow to follow the topography, causing the density field to oscillate vertically and, hence, act as a source of baroclinic energy. Maximum generation occurs at a region where the bottom slope matches the slope of the characteristics c (Baines 1974), given by

$$c \equiv \left(\frac{\omega^2 - f^2}{N^2(z) - \omega^2}\right)^{1/2} = \frac{dh}{dx}, \qquad (1)$$

where $N(z) = [-g/\rho_0 \partial\rho(z)/\partial z]^{1/2}$ is the buoyancy frequency $O(10^{-2})\ s^{-1}$, f the Coriolis parameter (here $1.08 \times 10^{-4}\ s^{-1}$), ω the tidal frequency ($1.41 \times 10^{-4}\ s^{-1}$), and $h(x)$ the bottom contour. Characteristics are ray paths along which internal wave energy propagates. The internal tide forcing is proportional to N^2. It is clear from Eq. (1) that real solutions exist only for $f < \omega < N(z)$. A suitable location for internal tide generation around smooth continental margins is at the shelf break not only because it may be tangential to the characteristics but also because it is located near the pycnocline where the density stratification is a maximum.

* Present Address: Laboratory of Meteorology and Oceanography, Department of Applied Physics, University of Athens.

Corresponding author address: P. G. Drakopoulos, Laboratory of Meteorology and Oceanography, Department of Applied Physics, University of Athens, 33 Ippocratous St., 10680, Athens, Greece.

Available internal tide models assume that the governing dynamics are those of a vertically stratified, rotating, and incompressible Boussinesq fluid:

$$\frac{\partial \mathbf{u}}{\partial t} + 2\Omega \times \mathbf{u} + \frac{1}{\rho_0} \nabla p = -\frac{\rho}{\rho_0} g\hat{z} \tag{2a}$$

$$\frac{\partial \rho}{\partial t} = \frac{\rho_0 N^2}{g} w \tag{2b}$$

$$\nabla \cdot \mathbf{u} = 0, \tag{2c}$$

where $\mathbf{u} \equiv u\hat{x} + v\hat{y} + w\hat{z} \equiv \{u, v, w\}$ is the velocity vector, ρ_0 is a constant mean density, and ρ is a density perturbation. An implicit assumption in Eq. (2b) is that the internal tide wavelengths be large compared to the water depth, making the hydrostatic approximation valid. In addition, the longshore (y axis) variation is considered to be negligible compared to the cross-shore (x axis) for scales of the order of internal wave dynamics, and all derivatives with respect to y can be set equal to zero, leading to solutions describing a wave propagating cross-shore.

For a flat bottom, the vertical dependence can be separated from the horizontal and the velocities can be expressed as

$$\mathbf{u} \equiv \{u, v, w\} = A\left\{\frac{\omega}{k}\frac{\partial \psi}{\partial z}, -i\frac{f}{k}\frac{\partial \psi}{\partial z}, -i\omega\psi\right\}e^{i(kx-\omega t)}, \tag{3}$$

where $\psi(z)$ is a solution to the Sturm–Luiville equation:

$$\frac{\partial^2 \psi}{\partial z^2} + \frac{k^2}{c^2}\psi = 0, \tag{4}$$

with boundary conditions $\psi(0) = \psi(-h) = 0$. Here k is the horizontal wavenumber and c is the characteristic defined in Eq. (1). There are an infinite number of solutions (or normal modes) to this equation, each one corresponding to a different eigenvalue k. The wave can be described as a superposition of several modes with energy propagating in a beamlike pattern along the characteristics, away from the shelf break. This oversimplified two-dimensional picture of the internal tide has been observed in laboratory experiments, but comparison with field results has not always been successful (e.g., Wunsch 1975). Frictional and nonlinear effects eventually dissipate the higher modes, causing the beam structure to decay away from the generation region. Moreover, seasonal and spatial variability in the density stratification will modulate the amplitude of the internal wave through the modification of $N(z)$ and render the baroclinic tide intermittent. One should not, therefore, expect the existence of a simple pattern capable of describing oceanic internal tides, and as a consequence, the task of identifying them becomes difficult. Recently, Pingree and New (1989, 1991) were successful in locating a beam of internal tide energy and tracing it beyond the point of bottom reflection. This was done in the Bay of Biscay, where the semidiurnal baroclinic current reaches values as high as 1.0 m s^{-1}, and thus, the signal of the internal tide is strong.

A characteristic common to most internal tide investigations is the scarcity of the data examined. Marsden (1986) examines only 22 days of data on Georges Bank; Pingree and New (1989, 1991) are limited to 10 days of data; while Barbee (1975) is limited to a mooring of four temperature sensors deployed for a period of 28 days. Although the intermittent nature of the internal tide is well known, a comprehensive documentation of this evolution over the annual cycle has not been well documented. The west coast of Vancouver Island offers an excellent opportunity to assess the seasonal evolution of the internal tide. Typically during winter, the weather patterns are dominated by the Aleutian low, leading to winds that produce downwelling at the coast. During the late spring, the winds reverse creating upwelling—leading to marked deflection in the isopycnals and hence, the beam characteristic paths. In this study, 18 months of current meter and hydrographic data will be examined to show the effect of reversing winds and changing density structures on the generation of the internal tide. The paper will be organized as follows. In section 2, the physical setting and the available data are presented. This is followed by a description in section 3 of the methods used to extract the baroclinic velocity field. In section 4, features of the internal tide are analyzed through ray tracing and empirical orthogonal function analysis. Internal tide properties are deduced including: direction of propagation, generation regions, beam structure, and spatial coherence. The EOF analysis results are compared in section 5 with a modified version of a model by Prinsenberg and Rattray (1975). Finally, section 6, addresses the possibility of interaction between the internal tide and an eddy present in the area during August 1980.

2. Observations

Current meter, temperature, and salinity records collected during the CODE experiment, conducted from May 1979 to September 1980 were used for the present study. In all, there were 41 current meters deployed in three cross-shelf sections, stretching from near shore to 80 km from the continental slope and consisting of a northern section situated off Brooks Peninsula, a central section off Estevan Point and a southern section off Carmanah Point (sections B0, E0, and CZ, respectively, see Fig. 1). Current meters used were Aanderaa RCM4s, Geodyne 850s, and CMDR. During the same period, seven large-scale hydrographic surveys were undertaken and the density data were used for estimating buoyancy frequencies. The CODE database was supplemented with current meter records from the Vancouver Island Coastal Current Experiment. This

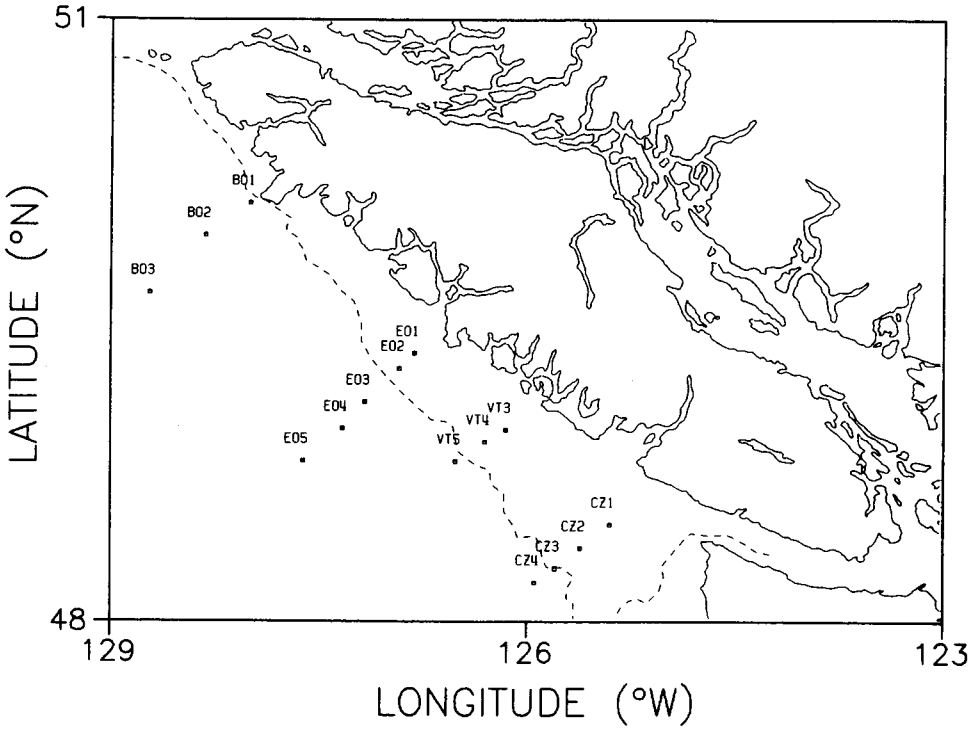

FIG. 1. The location of moorings for this study. The dotted line is the 200-m isobath indicating the shelf break (i.e., critical topography).

experiment extended over four months during the summer of 1984 with nine current meters deployed on the shelf. One section, located off Tofino and denoted here as VT, was analyzed. Two hydrographic surveys were undertaken during this time span. The periods of deployment and depths of all current meters on all moorings used in this work are displayed in Fig. 2.

Data collected from section E proved to be the most useful for detailed analysis. First, over 50% of the data were sampled from this section, providing the best temporal resolution of the four sections. Second, section E was the most favorable topographically as the continental shelf width is not uniform along Vancouver Island. At section B it is only 10 km wide, making it suitable only for a slope analysis. At sections CZ and VT it is between 50 km and 80 km wide. At section E the shelf and slope regions were of equal extent, with complete instrument coverage giving this section the best spatial resolution. Third, the coastline at section E is relatively straight and the bottom topography is relatively smooth, while at the other three sections there are large irregularities in both the cross-shore and alongshore directions (Figs. 1 and 3). As a result, the possibility exists at the other three sections that more than one generation region exist, thereby increasing the complexity of the analysis. Although similar analyses were performed on all the data, special emphasis is given to data collected along section E, particularly for verification of the theory.

3. Analysis

a. Harmonic analysis

To ensure a common time step, all the current meter records were subsampled hourly. By filtering the resultant time series with an 8-pole Butterworth bandpass filter centered at the M_2 frequency, intermittent (modulated) speed and temperature patterns were revealed for most records as shown in Fig. 4. Clearly the amplitude varies from about 0.01° to 0.07°C; thus, in order to resolve this variability it was necessary to perform an harmonic analysis on record blocks. To obtain the tidal coefficients (amplitudes and Greenwich phase lags), a standard harmonic analysis was performed according to Foreman (1978). The block size chosen was 15 days (effective bandwidth B_e = 0.003 cph), which was large enough to resolve the M_2 from the S_2 constituent, (Δf = 0.0033 cph). The blocks had a 14-day overlap; that is, the analysis was done for every day in order to obtain a better temporal representation of the speed variability.

b. Spectral analysis

More insight into the baroclinic field behavior can be obtained using spectral analysis techniques on the time series of harmonic coefficients. Each complex M_2 coefficient (amplitude and phase) can be considered as an ensemble of the same stochastic process, and

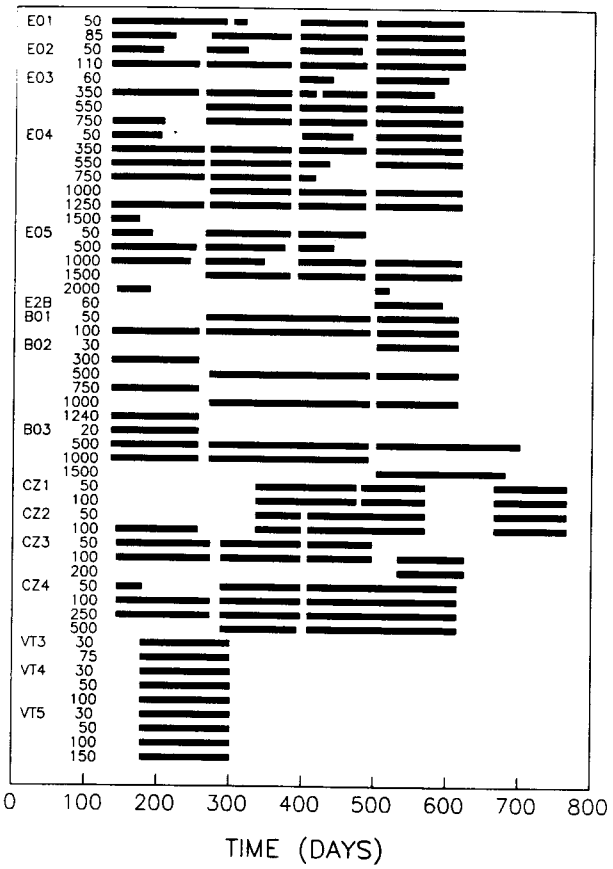

FIG. 2. Deployment times for the instruments as a function of location and depth. The year is 1979 except for section VT where the start year is 1984.

standard spectral averaging can be performed. A coherence squared function c_{ab} between two such complex coefficients $\hat{a}$ and $\hat{b}$ is given by

$$c_{ab} = \frac{|\sum_j \hat{b}_j \hat{a}_j^*|^2}{\sum_j \hat{a}_j \hat{a}_j^* \sum_j \hat{b}_j \hat{b}_j^*}, \quad (5)$$

with the hat denoting a complex quantity and the asterisk a complex conjugate. The value s for which c_{ab} is significantly greater than zero (95% confidence level) is obtained from

$$s = 1 - (0.05)^h, \quad (6)$$

with $h = 1/(n-1)$, n being the degrees of freedom (Groves and Hannon 1968). In order to compensate for the overlap of the blocks, the equivalent degrees of freedom were set equal to $n = (2q + 28)/15$, where q is the number of ensembles considered in each case. Following the same principle, a transfer function between $\hat{a}$ and $\hat{b}$ can be defined as

$$\hat{t}_{ab} = \frac{\sum_j \hat{b}_j \hat{a}_j^*}{\sum_j \hat{a}_j \hat{a}_j^*}. \quad (7)$$

The absolute value of $\hat{t}_{ab}$ represents the gain of the system while the phase g_{ab} indicates the overall phase relationship (polarization) of the two sets of coefficients. In order to reduce the overall error, the data were weighted by the variances obtained by the least-squares fitting during the harmonic-analysis procedure. Between v and u the gain t_{vu}, the cross-spectral phase g_{vu}, and the coherence c_{vu} were calculated. The first parameter represents the amplitude relationship, the second their phase relationship, and the third the degree to which they are phase locked. Furthermore, between barotropic and baroclinic cross-shore components, the coherence c_u and the corresponding phase g_u were calculated. The coherence describes the internal tide variability, while the phase gives an indication of the baroclinic cross-shore phase propagation, since the barotropic field is constant. In order to deduce horizontal–vertical field relationships and since temperature oscillations represent vertical motion, the cross-spectral phase g_t between temperature and barotropic field, the phase g_{tu} and coherence c_{tu} between temperature and horizontal baroclinic field were also calculated.

c. *Baroclinic horizontal velocities*

The amplitudes and phases obtained from the harmonic analysis represent a superposition of barotropic and baroclinic components, and a further step to remove the barotropic component is required. Various methods of isolating the internal tide are implemented in the literature. The barotropic tide being a shallow-water wave has, ignoring friction effects, a constant horizontal velocity field as a function of depth. Therefore, a simple vector subtraction of the barotropic coefficients from the total yields the baroclinic component. For the present case, three independent sets of M_2 coefficients for the surface tide were employed in the analysis. The first two sets were obtained from two numerical models that exist for the region by Flather (1988) (which will be referred to as T_1) and Foreman and Walters (1990) (T_2) following the extraction technique of Marsden (1986). The quality of output from numerical models is sensitive to the values selected for the model friction, eddy viscosity, and eddy diffusivity coefficients, and to a possible lack of resolution of the sloping bottom topography. The third set was deduced from the actual field data (referred to as T_3). By performing a harmonic analysis on total records ($\sim$1 year), the expected incoherence of the internal tide will force it to have a negligible effect on the tidal coefficients. Moreover, depth averaging of these parameters will even further diminish residuals of the baroclinic component. This technique is sensitive to long-term

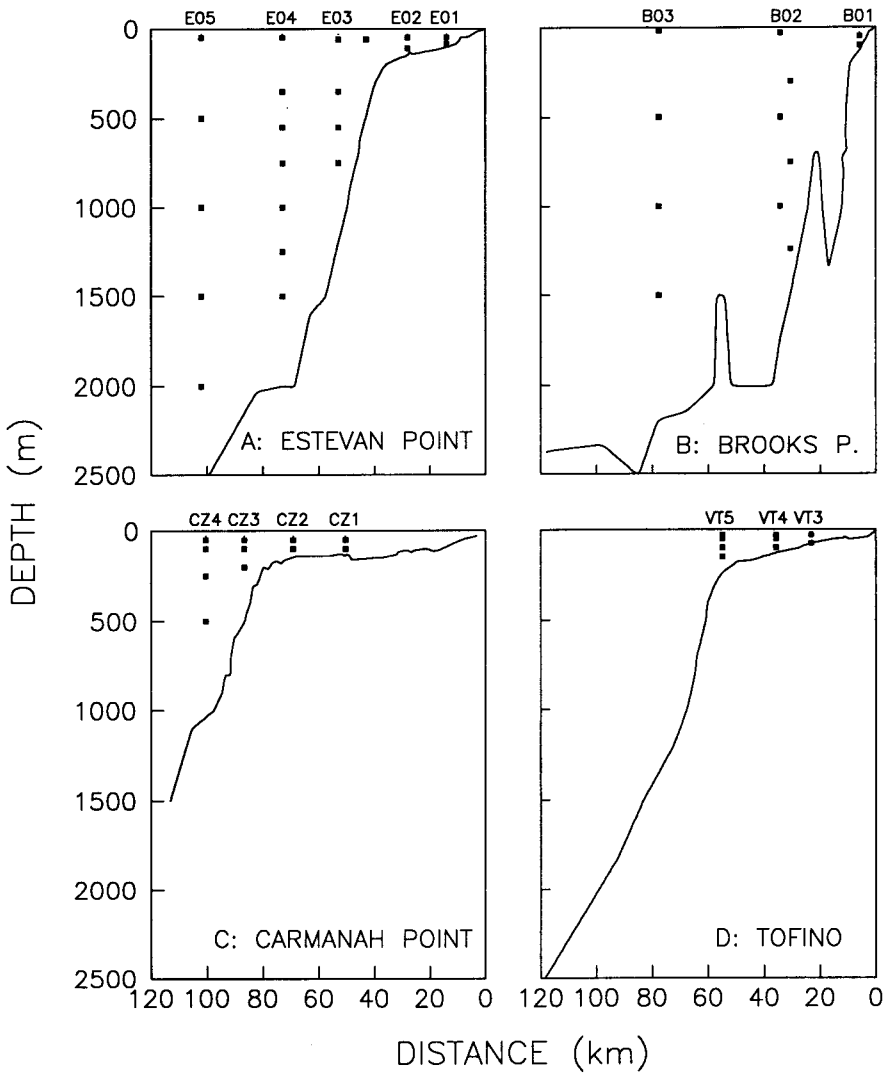

FIG. 3. Bottom cross sections and current meter locations for the four sites under investigation: (a) Estevan Point, (b) Brooks Peninsula, (c) Carmanah Point, and (d) Tofino.

generation of the internal tide and may be most inaccurate near the generation region. The three sets of M_2 barotropic coefficients for every location are listed in Table 1. It is apparent that the three methods do not produce identical results. After subtracting the estimates of the barotropic M_2 tidal velocity coefficients from the experimental values, the resulting currents were assumed to represent the baroclinic field superimposed with some noise and possibly a barotropic residual. The Cartesian coordinates were then rotated so that the y axis was aligned with the local isobath contours so that u and v represent the cross-shore and alongshore velocity components, respectively.

The transfer function between v and u can be used to estimate the direction of propagation of the internal tide. According to internal wave dynamics and assuming a plane wave propagating in a direction at an angle θ with the x axis, from the momentum equations we obtain

$$r = \frac{v}{u} = \frac{i \sin\theta + f/\omega \cos\theta}{i \cos\theta - f/\omega \sin\theta}. \tag{8}$$

Thus, for M_2 propagation along the x axis (cross-shore), it is expected that the amplitude of the ratio (r) be 0.8 and the phase of u lead that of v by 90°. However, the results were found to be very sensitive to the barotropic model used. Levine and Richman (1989) considered the velocity differences at the same coordinate but at different depths according to

$$\Delta u = u(x_1, y_1, z_1) - u(x_1, y_1, z_2)$$

$$\Delta v = v(x_1, y_1, z_1) - v(x_1, y_1, z_2).$$

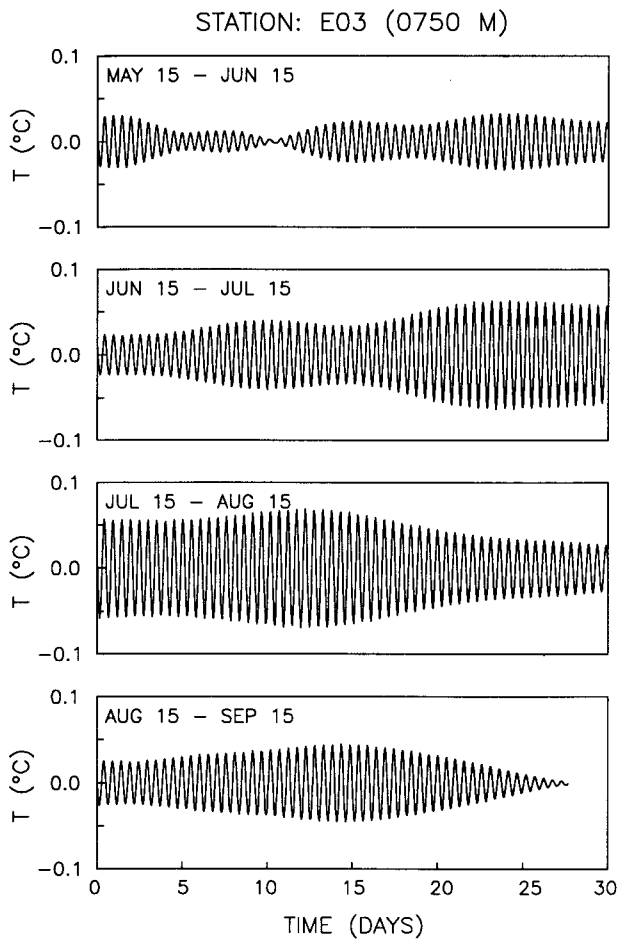

FIG. 4. Filtered temperature time series with an 8-pole Buterworth filter centered at the M_2 frequency.

The ratio $r = \Delta v / \Delta u$ is identical to Eq. (8) for all depth combinations, assuming that the internal tide consists of a single plane wave. The ratio is also independent of the barotropic model and can be used to verify the T_1, T_2, and T_3 results. To increase the confidence in the estimate, all possible depth differences for a particular location were vectorially depth averaged; that is, one data value for each mooring was obtained. Similarly, the complex transfer functions obtained by the models, T_1, T_2, and T_3 were depth averaged. The amplitude phase contour implied by Eq. (8), along with the experimental data for all available methods and sections are plotted in Figs. 5a–d. The abscissa and ordinate represent the amplitude and phase of the ratio of Eq. (8). The curve is the set of allowable values for the propagation of a single plane wave. The numbers superimposed on the curve give the propagation directions (θ) with 0° being cross-shore and 90° being alongshore propagation. Note that the ratio has a 180° ambiguity. For B and E sections, all three sets indicate a cross-shore propagation, with the exception of B01 mooring (near the shore), where it appears that the internal wave is far from a simple plane wave relationship. At section CZ propagation within a cone of 90° centered on the onshore–offshore axis is indicated. The Foreman and Walters (1990) (triangles) T_2 method produces an overestimate of the alongshore baroclinic velocity. For the VT section near shore, the values obtained cannot be described by a simple plane wave, but elsewhere cross-shore propagation is indicated by the differences technique (circles) and experimental average method (T_3). Again, however, the T_2 method gives radically different hodographs. Following these observations, and considering the amount of scatter of

TABLE 1. Parameters for the M_2 barotropic tide as obtained by two numerical models and from the CODE experiment; u is directed across shore and v alongshore. Units for amplitudes are centimeters per second, and the Greenwhich phase lags are in degrees for Pacific Standard Time.

	Flather (T_1)				Foreman (T_2)				Experiment (T_3)			
Mooring	u (cm s^{-1})	g_u (deg)	v (cm s^{-1})	g_v (deg)	u (cm s^{-1})	g_u (deg)	v (cm s^{-1})	g_v (deg)	u (cm s^{-1})	g_u (deg)	v (cm s^{-1})	g_v (deg)
B01	1.0	20.5	3.0	309.1	—	—	—	—	1.4	296.3	2.8	316.6
B02	0.7	290.7	2.6	327.6	—	—	—	—	0.6	50.4	3.2	345.7
B03	0.8	285.4	2.6	332.9	—	—	—	—	1.3	253.0	1.5	13.9
E01	3.2	279.1	1.4	302.6	—	—	—	—	1.7	233.5	3.6	10.9
E02	3.2	276.9	1.1	312.9	—	—	—	—	3.6	288.5	1.0	288.5
E03	0.9	308.1	2.5	329.3	—	—	—	—	0.7	231.2	1.9	345.4
E04	0.9	302.4	2.5	331.5	—	—	—	—	0.9	288.0	1.8	333.8
E05	1.0	305.0	2.6	331.0	—	—	—	—	1.4	313.0	2.1	324.1
CZ1	5.3	46.0	6.4	275.3	5.9	33.7	8.7	257.8	7.6	18.8	7.0	257.7
CZ2	4.7	38.5	4.9	290.7	5.5	17.2	7.3	265.3	6.0	28.8	5.6	286.1
CZ3	1.3	16.7	2.7	306.3	3.1	355.1	5.4	264.6	2.9	40.3	3.7	315.5
CZ4	0.7	8.5	2.1	317.3	1.8	332.2	4.3	265.9	0.2	51.3	0.9	317.2
VT3	—	—	—	—	2.8	322.0	8.6	286.5	1.1	231.1	3.8	283.5
VT4	—	—	—	—	3.3	332.2	7.9	289.1	1.3	297.9	4.3	279.5
VT5	—	—	—	—	2.4	355.5	6.6	296.6	2.6	300.0	5.0	263.7

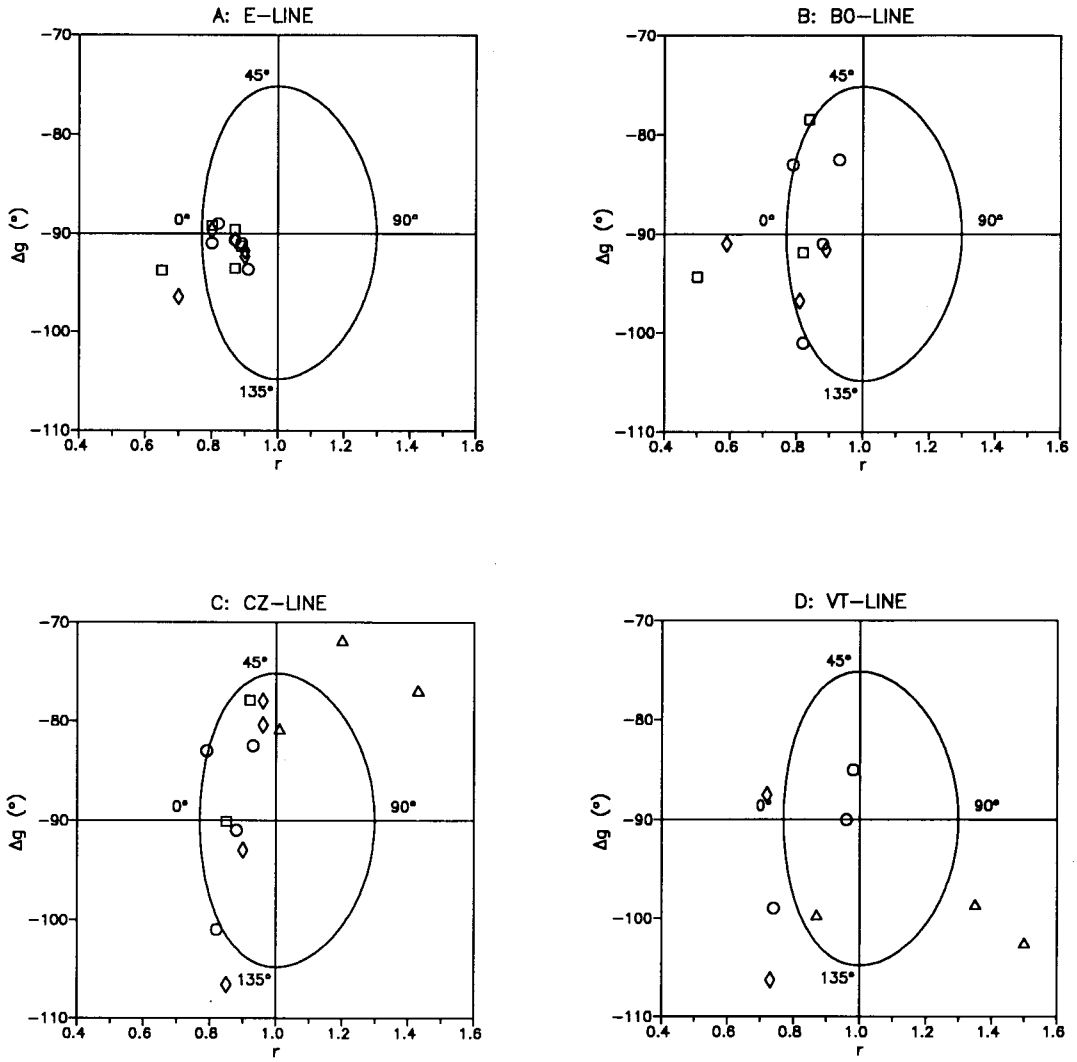

FIG. 5. Contour of allowed values for the alongshore: cross-shore ratio–phase difference pair. Superimposed are field results obtained using the three different methods to subtract the barotropic component; the squares refer to the Flather (1988) (T_1) model, triangles to the Foreman and Walters (1990) (T_2) model, and rhombs to the experimental (T_3) method. The circles refer to the difference method of Levine and Richman (1989), which is independent of a barotropic velocity estimate. Figure 5(a) is section E, (b) section B, (c) section CZ, and (d) section VT.

the data for each method, the remainder of the paper will be carried out based on Flather's model (T_1) for sections B, E, CZ, and the experimental average method (T_3) for section VT.

d. Vertical velocities

To estimate the vertical velocity field, temperature and salinity records were used. If the heat conduction and diffusion coefficients are disregarded, and the assumption is made that the horizontal temperature or salinity gradient vanishes, then the vertical velocity is given by

$$w = -\frac{\partial T/\partial t}{\partial \langle T \rangle/\partial z} = -\frac{\partial S/\partial t}{\partial \langle S \rangle/\partial z}, \tag{9}$$

where the brackets represent long-term mean values. The temperature and salinity records were obtained from the sensors on the current meters, while the vertical gradients were estimated from the CTD observations. This technique can easily be erroneous when the stratification is weak and the vertical gradient becomes negligible. In addition, the value of the vertical gradient will also depend on the phase of the tidal cycle during which the CTD observation was made. Both salinity and temperature records gave comparable results, but the temperature records were less sensitive

to fluctuations in freshwater runoff from Vancouver Island and the Strait of Juan de Fuca and were preferred for the analysis where possible.

4. Results and discussion

a. *Tidal coefficient time series*

There were 52 instrument records processed with the procedures outlined in the previous section, and representative outcomes using Flather's barotropic model (T_1), can be seen in Fig. 6. Four parameters are displayed: the cross-shore velocity, its corresponding Greenwhich phase lag, the ratio of alongshore velocity amplitude to that of the cross-shore $r = v/u$, and their phase difference $\Delta g = g_v - g_u$. The figure shows a highly intermittent velocity field. During winter the baroclinic energy is low while it peaks in the summer to values much larger than the barotropic forcing field. Furthermore, substantial baroclinic tidal velocities are seen to 750-m depth. The period of largest fluctuations in r and Δg occur from days 400 to 450 corresponding to the period from February to April 1980—again when the internal tide signal is smallest. It must be emphasized that Fig. 6 is representative of the entire dataset. For example, on the shelf off Brooks Peninsula total horizontal baroclinic speeds [i.e., $(u^2 + v^2)^{1/2}$] as high as 22.0 cm s^{-1} have been measured with corresponding barotropic velocities of only 3.2 cm s^{-1}. Likewise, off Estevan Point speeds of 15.0 cm s^{-1} (2.7 cm s^{-1} for barotropic velocity) and 14.0 cm s^{-1} at CZ line (2.2 cm s^{-1} for the barotropic velocity) have been measured (see Table 2). For most cases, the amplitude of r has a bias toward values larger than 0.8. Similar observations were made by Huthnance and Baines (1982) for the internal tide off northwest Africa, which they attribute to the presence of a viscous boundary layer near the bottom. Elsewhere a different mechanism has to be responsible. One possibility is mean flow–internal wave interaction (e.g., Kundu et al. 1988). The internal tide can act as an eddy viscosity for the low-frequency motions, extracting kinetic energy. For most sites, the

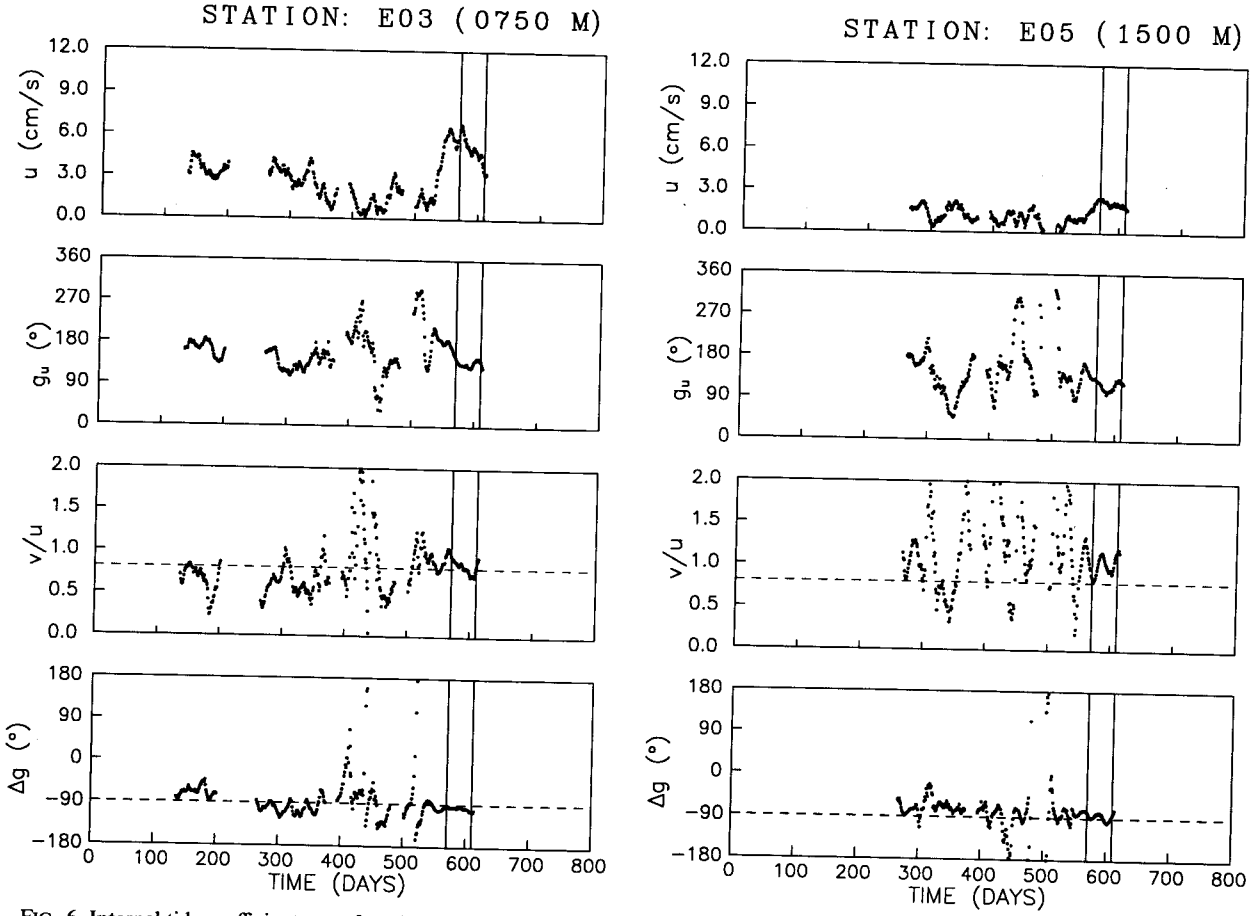

FIG. 6. Internal tide coefficients as a function of Julian day for E section: (a) over the continental slope and (b) in the deep ocean. Day 1 is 1 January 1979. Four coefficients are displayed: cross-shore velocity amplitude, corresponding Greenwich phase lag for PST, ratio of alongshore to cross-shore amplitude, and their phase difference. The dashed lines are theoretical values. The vertical lines indicate the time span of an eddy present in the area.

TABLE 2. Spectral analysis results for M_2 baroclinic parameters. The letters t, g, c, and s denote gain, phase, coherence, and 95% level of significance, respectively, while the subscripts indicate the input and output of the system. The degrees of freedom are variable for each location depending on the total amount of available data (60 d.f. maximum).

Mooring	Depth (m)	u_{max} (cm s^{-1})	v_{max} (cm s^{-1})	t_{vu}	g_{vu} (deg)	c_{vu}	c_u	g_u (deg)	s_{vu}	g_t	g_{tu} (deg)	c_{tu}	s_{tu}
						Winter							
E01	50	3.6	5.7	0.3	−160	0.0	0.1	285	0.2	9	−78	0.0	0.2
	85	4.9	4.2	0.6	−117	0.3	0.1	156	0.1	157	61	0.1	0.1
E02	50	5.7	5.9	1.0	−72	0.8	0.6	87	0.2	74	−30	0.0	0.2
	110	5.1	3.7	0.8	−99	0.8	0.2	291	0.1	177	−107	0.3	0.1
E03	60	4.0	4.0	1.0	−72	0.8	0.2	48	0.4	215	−168	0.4	0.4
	350	3.3	3.5	1.2	−92	0.8	0.3	221	0.1	277	−167	0.1	0.2
	550	5.1	3.8	0.8	−79	0.9	0.4	167	0.1	98	−94	0.5	0.1
	750	4.3	2.5	0.6	−102	0.8	0.6	137	0.1	102	−74	0.4	0.1
E04	50	5.2	6.1	0.9	−65	0.9	0.6	87	0.3	—	—	—	—
	350	2.3	3.8	1.2	−94	0.5	0.1	280	0.1	250	−20	0.1	0.1
	550	2.8	3.7	1.2	−103	0.9	0.4	308	0.2	199	−110	0.0	0.2
	750	1.9	2.4	0.5	−108	0.2	0.3	3	0.2	207	−157	0.0	0.2
	1000	4.2	3.7	0.9	−81	0.9	0.3	130	0.1	54	−130	0.2	0.1
	1250	4.3	4.0	0.8	−77	0.8	0.6	184	0.1	113	−79	0.5	0.1
	1500	—	—	—	—	—	—	—	—	—	—	—	—
E05	50	7.7	7.7	1.0	−90	0.9	0.5	261	0.1	218	−47	0.5	0.1
	500	2.0	2.3	0.9	−82	0.4	0.0	293	0.2	—	—	—	—
	1000	3.2	2.4	0.7	−85	0.9	0.7	32	0.2	161	129	0.5	0.2
	1500	2.2	2.5	0.9	−76	0.7	0.3	130	0.1	168	83	0.3	0.1
	2000	—	—	—	—	—	—	—	—	—	—	—	—
E2B	60	—	—	—	—	—	—	—	—	—	—	—	—
						Summer							
E01	50	6.9	5.0	0.5	−93	0.3	0.0	275	0.1	223	−103	0.0	0.1
	85	10.8	10.0	0.9	−88	0.9	0.3	101	0.1	214	−138	0.3	0.1
E02	50	7.3	6.9	0.9	−88	0.9	0.3	171	0.1	53	−55	1.0	0.9
	110	7.1	4.9	0.6	−95	0.8	0.2	317	0.1	201	−170	0.3	0.1
E03	60	6.6	5.7	1.1	−95	0.9	0.2	33	0.2	123	33	0.4	0.2
	350	5.6	4.5	0.8	−101	0.7	0.3	344	0.1	50	−45	0.2	0.1
	550	3.7	4.7	1.0	−83	0.8	0.4	230	0.1	113	−124	0.4	0.1
	750	6.8	6.2	0.8	−91	0.9	0.7	160	0.1	77	−82	0.8	0.1
E04	50	10.8	10.0	0.9	−94	1.0	0.5	354	0.1	—	—	—	—
	350	3.2	3.9	1.1	−98	0.8	0.3	264	0.1	190	8	0.1	0.1
	550	4.3	4.1	1.0	−101	0.9	0.6	317	0.1	256	−8	0.1	0.1
	750	2.6	2.1	0.7	−109	0.5	0.5	7	0.1	297	−74	0.5	0.2
	1000	3.0	2.9	0.8	−89	0.9	0.4	71	0.1	53	−52	0.0	0.5
	1250	4.6	4.0	0.8	−87	0.9	0.5	176	0.1	113	−68	0.7	0.1
	1500	1.5	2.5	2.0	−2	0.9	0.9	143	0.4	—	—	—	—
E05	50	8.5	6.0	0.6	−96	0.7	0.3	332	0.2	214	−80	0.0	0.1
	500	3.5	3.4	1.0	−99	0.8	0.0	292	0.1	191	0	0.2	0.2
	1000	4.4	4.2	0.8	−93	0.9	0.4	38	0.1	169	136	0.5	0.1
	1500	2.5	2.7	1.0	−82	0.9	0.7	133	0.1	234	80	0.7	0.5
	2000	1.7	2.3	1.3	−11	0.8	0.9	118	0.3	—	—	—	—
E2B	60	5.9	6.3	1.0	−104	0.5	0.0	165	0.2	226	22	0.3	0.2
B01	50	9.4	7.6	0.6	−92	0.6	0.5	272	0.1	142	−139	0.1	0.1
	100	8.6	5.8	0.4	−98	0.2	0.1	155	0.0	11	101	0.4	0.0
B02	30	16.7	14.2	0.9	−84	1.0	0.8	310	0.2	167	−134	0.4	0.2
	300	4.8	5.1	1.0	101	0.9	0.5	278	0.2	221	−64	0.3	0.2
	500	3.5	4.1	0.9	−102	0.8	0.1	6	0.1	207	−113	0.1	0.1
	750	7.5	6.6	1.0	−92	1.0	0.8	106	0.2	39	−73	0.3	0.2
	1000	5.4	5.4	0.9	−82	0.9	0.6	102	0.1	49	−57	0.4	0.1
	1240	4.0	2.5	0.3	−84	0.3	0.3	17	0.2	217	−159	0.7	0.2
B03	20	12.6	11.4	0.8	−87	0.9	0.4	109	0.2	204	106	0.6	0.3
	500	4.0	4.4	1.0	−86	0.9	0.3	226	0.0	92	−133	0.2	0.0
	1000	3.6	4.0	1.0	−65	0.6	0.4	162	0.1	163	8	0.4	0.1
	1500	1.8	2.2	0.6	−77	0.2	0.1	78	0.1	140	56	0.2	0.1

TABLE 2. (*Continued*)

Mooring	Depth (m)	u_{max} (cm s^{-1})	v_{max} (cm s^{-1})	t_{vu}	g_{vu} (deg)	c_{vu}	c_u	g_u (deg)	s_{vu}	g_t	g_{tu} (deg)	c_{tu}	s_{tu}
CZ1	50	9.5	9.0	0.7	−116	0.8	0.3	340	0.1	35	21	0.0	0.1
	100	8.3	6.9	0.7	−122	0.7	0.4	332	0.1	112	117	0.3	0.1
CZ2	50	8.7	7.1	0.8	−88	0.8	0.6	11	0.1	123	−168	0.0	0.1
	100	7.3	7.4	0.9	−92	0.9	0.1	174	0.1	42	−77	0.1	0.1
CZ3	50	6.7	6.7	0.9	−86	0.9	0.2	62	0.1	199	136	0.1	0.1
	100	5.4	5.1	0.8	−75	0.8	0.4	60	0.1	232	157	0.2	0.1
	200	3.0	4.2	1.1	−49	0.6	0.2	93	0.2	124	−38	0.3	0.2
CZ4	50	8.8	10.5	0.9	−82	0.8	0.3	188	0.1	162	−37	0.0	0.1
	100	6.7	8.5	1.0	−82	0.8	0.0	155	0.1	204	58	0.0	0.1
	250	5.1	5.8	0.9	−71	0.7	0.3	81	0.1	181	40	0.1	0.1
	500	4.1	5.3	0.9	−76	0.6	0.4	315	0.1	204	−97	0.3	0.1
VT3	30	5.9	4.9	0.3	−121	0.2	0.4	292	0.2	—	—	—	—
	75	5.8	5.3	0.5	−126	0.4	0.3	291	0.2	—	—	—	—
VT4	30	9.5	7.9	0.7	−97	0.8	0.5	291	0.2	—	—	—	—
	50	5.7	4.4	0.6	−119	0.5	0.6	281	0.2	—	—	—	—
	100	4.9	6.5	0.9	−105	0.6	0.1	217	0.2	—	—	—	—
VT5	30	9.7	9.0	1.0	−108	0.9	0.7	223	0.2	—	—	—	—
	50	9.5	10.2	0.9	−115	0.9	0.7	244	0.2	—	—	—	—
	100	7.8	4.9	0.5	−88	0.7	0.6	299	0.2	—	—	—	—
	150	6.6	5.4	1.0	−37	0.7	0.6	14	0.2	—	—	—	—

phase difference Δg appears to be very close to the theoretical value of $-90.0° \pm 10.0°$ indicative of cross-shelf propagation. The few instances for which a different phase was found occurred when the estimated cross-shelf baroclinic velocity was less than 2.0 cm s^{-1} and was coincident with a large scatter in the amplitude of the ratio r. Figure 7 shows the amplitude and phase differences for representative temperature fluctuations. Again, the phase differences are close to the theoretical values, indicative of cross-shelf propagation. Deviations occur mostly when the amplitude of the vertical fluctuation is small.

Figures 8a and 8b show representative hydrographic sections, in situ densities, at section E for January and early September of 1980. The summer maximum and winter minimum in internal wave amplitude follows the seasonal density stratification of the top 200-m water mass, that is, water well stratified during the summer and well mixed during the winter. From hydrographic data sampled near the shelf break during winter $N^2_{max} \approx 4 \times 10^{-3}$ s^{-2}, while during summer $N^2_{max} \approx 9 \times 10^{-3}$ s^{-2}, which, according to Baines (1974) would account for increased forcing of the baroclinic field. Furthermore, at the shelf break, there is a marked downwelling evident in the isotherms in January and a marked upwelling in September, due to the shift in the wind pattern.

The results can be quantified further through the spectral analysis techniques outlined in section 3. Table 2 contains the bulk transfer functions, phases, and coherences for all stations at all depths. Section E data have been divided into winter and summer seasons. At section E, all the statistics indicate larger velocities and higher velocity coherences (c_{uv}) during the summer. Furthermore, the transfer function amplitudes are mostly less than 1.0 and, hence, consistent with cross-shelf propagation. Again, the bulk phase angles are generally closer to the theoretical −90.0° in summer than in winter. The bulk cross-shore/temperature coherences (c_{tu}) are generally much smaller than the velocity coherences but are also larger in summer than in winter. At section B, both the (c_{uv}) and (c_{tu}) coherences are again quite high, although the temperature/velocity phases (g_{tu}) show considerable scatter about the expected value of −90.0°. At section CZ, the velocity coherences (c_{tu}) are, however, very small and in some instances, are less than the noise level indicated by s_{tu}. Finally, the section VT velocity coherences are the smallest of any location. At all sections, the moorings nearest shore (01 locations) have smaller coherences than those farther offshore.

b. Generation regions and beam structure

Potential generation regions for the internal tide, according to Baines (1974), are where the bottom is tangent to the characteristic ray. The ray paths emanating from the generation region(s) indicate locations of maximum expected internal tide energy. Taking into account horizontal density gradients and following Mooers (1973), Eq. (1) for the slope of the characteristics becomes

$$c = \frac{M^2 \pm \{M^4 + [\omega^2 - f(f + \partial v/\partial x)](N^2 - \omega^2)\}^{1/2}}{(N^2 - \omega^2)}, \quad (10)$$

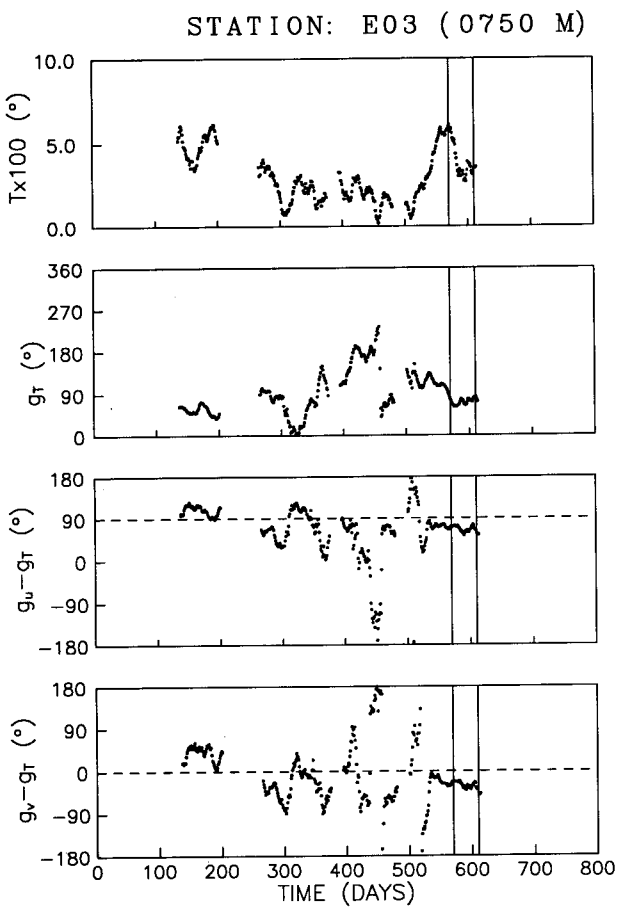

FIG. 7. Same as in Fig. 6 but showing temperature semidiurnal coefficients for the mooring over the continental slope. Four parameters are displayed: amplitude, corresponding phase, phase difference with cross-shore velocity, and phase difference with alongshore velocity. Dashed lines represent values expected for plane internal waves. The vertical lines indicate the time span of an eddy present in the area.

where $M^2 = -(g/\rho)\partial\rho/\partial x$ is the horizontal analog of the buoyancy frequency. Using CTD information for summer and winter, and neglecting the cross-shore gradient of the mean alongshore flow, since it was found to be negligible, this equation was used to trace rays emanating from the shelf break.

The resolved velocity field pattern is expected to be more conclusive at section E where the most intense sampling occurred. On the shelf, the mooring located nearest to the shelf break is E02. The shoreward ray emanating from the shelf break (Fig. 9a) appears to pass near the 50-m current meter. Table 2 indicates that for both the velocity and temperature records, the amplitudes and coherences were high at mooring E02 50 m. Near shore, the coherences were low at mooring E01 50 m. The summer analysis shows, however, a marked increase in maximum velocity and coherence at E01 85 m. On the slope, the mooring near the primary generation region is E03. Figure 9a indicates that during winter, the ray passes near 550 m, while during summer it is close to 750 m. This can be readily verified in Table 2. At 550 m, during winter, with low stratification and weaker internal tide generation, the cross-shore velocity reaches values of 5.1 cm s^{-1} while during summer it decreases to 3.7 cm s^{-1}. In contrast, at a depth of 750 m during winter, the cross-shore velocity is only 4.3 cm s^{-1}, increasing to 6.8 cm s^{-1} during the summer. Similarly, estimating vertical velocity from the temperature time series and CTD casts, average values of 0.14 cm s^{-1} and 0.09 cm s^{-1} for moorings at 550 m and 750 m during winter are found. During summer the order reverses to 0.15 and 0.18 cm s^{-1}, respectively. Moreover, coherences between temperature and horizontal velocity follow the same pattern. Thus, during winter c_{tu} is higher at 550 m compared to that at 750 m, whereas the opposite is true for summer. Near the surface (60 m), the internal tide has cross-shore (vertical) velocities 4.0 (0.03) cm s^{-1} during winter and 6.6 (0.04) cm s^{-1} during summer. The propagation of the cross-shore velocity phase at mooring E03 is clearly upward both during summer and winter, indicating that energy propagates downward and away from the slope toward the open ocean. The phase difference between temperature and cross-shore velocity (g_{tu}) can provide important information for the modal composition of the internal wave. For a single mode to be present, g_{tu} should be 0° or 180° (i.e., with the cross-shore velocity and vertical velocity in quadrature). When a large number of modes are present or equivalently a beam pattern exists, g_{tu} should be −90° at locations where a ray passes according to Baines (1974). During winter, the phase is very close to −90° at depth 550 m, whereas for summer this is true at a depth of 750 m, another indication of the presence of a ray with a seasonal modulation of its path. For the near-surface current meter, this pattern cannot be verified. Off the shelf at mooring E04, the higher modes are expected to be dissipated, and those that remain lose their phase locking. Assuming an infinite number of modes, during winter the 350-m and 1250-m locations should be more energetic, while during summer this should shift to 50 m and 1500 m, respectively. This cannot, however, be verified in Table 2. Although the ratio of cross-shore velocity at 50 and 350 m is seasonally modified according to the beam pattern, the speeds remain stronger at 50 m year around. This suggests that at least during winter only a few modes survive and the velocities remain strong near the surface. Unfortunately, the temperature sensor at E04 50 m and 1500 m failed to return data during the summer. However, at 1250 m both the horizontal and vertical fields are strong and highly coherent year round. This indicates that energy might emanate from a different generation region. From the bottom topography (Fig. 9a) we see that the feature located 60 km

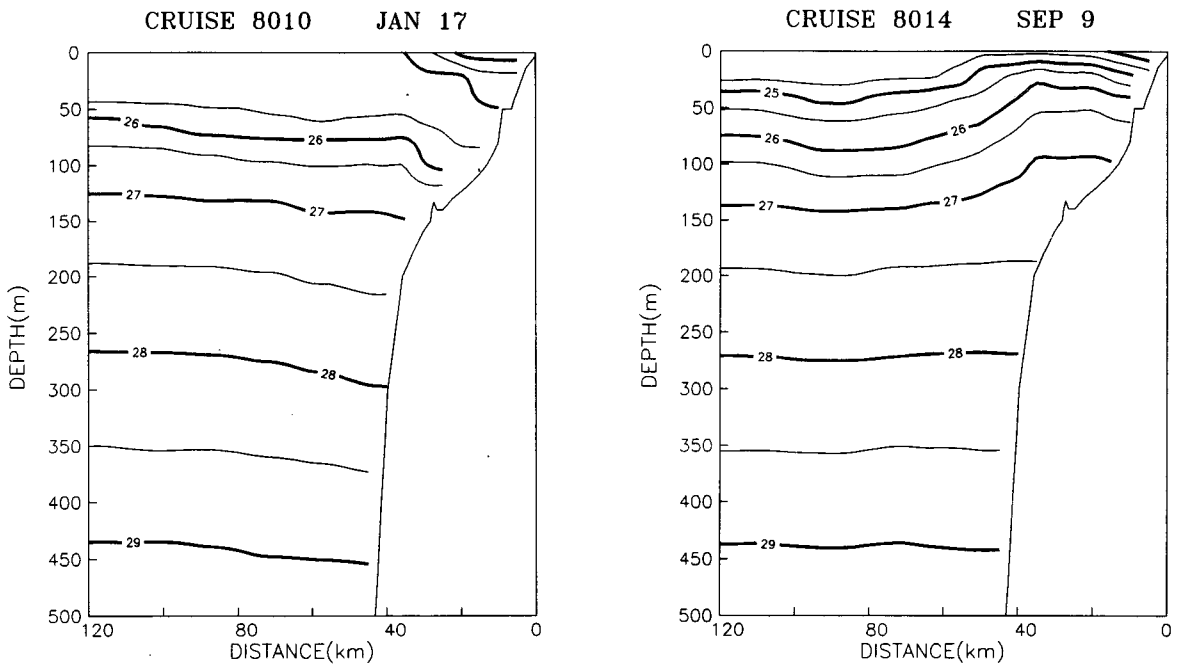

FIG. 8. Density stratification for E section as was computed from CTD casts for (a) January 1980 and (b) September 1980.

from the shore can be a generation region of a ray that intersects the mooring at 1250-m depth during the winter. For mooring E05, the energetic regions are at depths 50 m and 1000 m. The ray trace indicates that this is a reasonable pattern. An evaluation of coherences between records at different moorings and depths (not shown) suggested that the energy at 1000 m was highly coherent with station E04 50 m, while E05 50 m, although very energetic during summer, showed coherence with other moorings only during the winter.

For the section off Brooks Peninsula the database is much smaller and a seasonal analysis is not possible. Moreover, due to the complicated bathymetry there are a number of possible generation regions confusing the picture. Generally, the slope is supercritical (steeper than the characteristics), whereas the shelf appears to be almost critical. Figure 9b indicates that maximum activity is expected at B02 30 m all year, B02 750 m during winter, B02 1000 m during summer, and B03 1000 m all year. The maximum velocities and the $u - t(t_{ut})$ gain from Table 2, indicate that this is true for mooring B02; however, no winter current data were available at 750 m to observe a seasonal pattern. Even during summer the velocity field is stronger at 750 m; probably the result of constructive interference with rays emanating from the sharp bottom feature located approximately 20 km from the coast. The coherences between temperature and cross-shore velocity, cross-shore velocity and barotropic tide, and the two horizontal components are high along the ray path. At location B03 the expected beam pattern is not confirmed by the magnitude of the horizontal velocity field. Still there is an indication of downward propagation of energy, and the temperature–current coherence is high at 1000 m where the beam is supposed to pass. For the shelf, c_{tu} is high at the 100-m instrument, in agreement with the ray theory. A coherence analysis between locations (not shown) indicated a high coherence between the cross-shore velocities on the shelf and those at B02 750 and B02 1000 m.

The moorings along the CZ section cover half of the seaward shelf (CZ1, CZ2) and the slope (CZ3, CZ4). The temperature records were very noisy and the temperature–cross-shore velocity coherences were very low. The velocities at each mooring decrease with depth, indicating an absence of beam structure. At moorings CZ2 and CZ1, for both winter and summer, the beam is expected to pass at depth of 50 m. (Fig. 9c). The temperature–velocity coherences, however, indicate otherwise. The strongest temperature–velocity coherences are found at moorings CZ3 100 m and CZ4 500 m, in contradiction with the velocity results, and in rough agreement with the expected beam pattern. Horizontal velocity phase propagation at location CZ4 is upward, indicating a downward energy propagation also in agreement with the ray path analysis.

Due to limited data, it is impossible to extract a comprehensive picture for the baroclinic currents for section VT. The shelf is subcritical for the semidiurnal frequency, and a single ray emanating from the break should propagate onshore. At mooring VT5, closest to the generation region (Fig. 9d), the currents are much

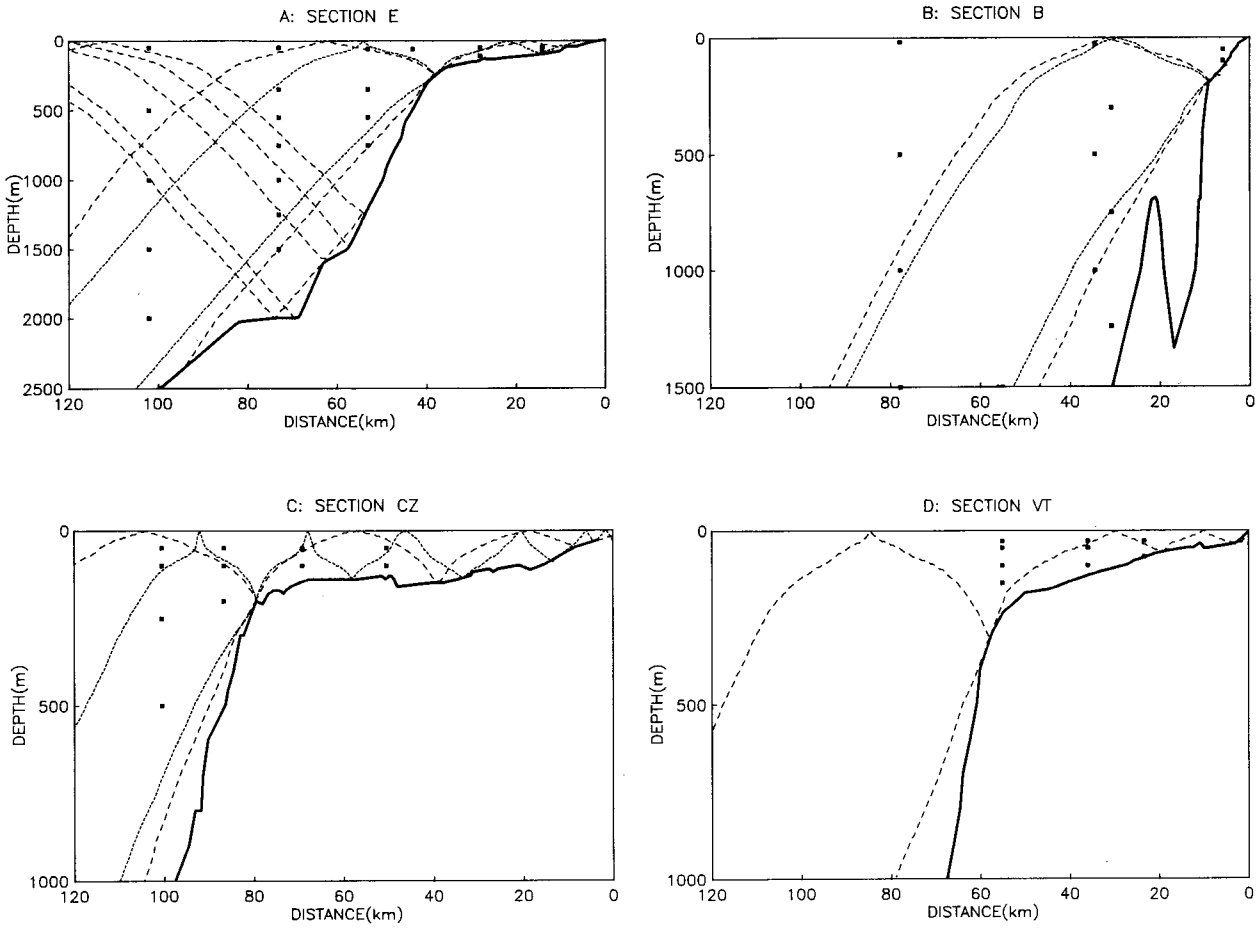

FIG. 9. Ray traces for the semidiurnal frequency and stratification corresponding to winter (dotted line) and summer (dashed line) conditions: (a) section E, (b) section B, (c) section CZ, and (d) section VT.

stronger near the surface, although the ray is expected to pass near the mooring at a depth of 150 m. The phase propagation is downward, which suggests that energy is propagating upward, in agreement with a generation region at the shelf break. At mooring VT4, the velocities are again larger near the surface and the phase propagates upward contradicting the ray of Fig. 9d. It seems that if a beam is really present, it passes at a depth of 100 m at mooring VT5 and then reflects at the surface before it reaches mooring VT4.

c. *EOF analysis*

An empirical orthogonal function (EOF) analysis was performed on the spatial-coherence matrix for section E during a two-month period [10 degrees of freedom (d.f.)] for both summer and winter. This analysis defines a statistical rotation of the data to a set of mutually incoherent modes. Each eigenvalue characterizes the total M_2 power contained in the mode. The hermitian M_2 cross-spectral matrix was constructed with elements defined by the numerator of Eq. (5) using both cross-shore and alongshore baroclinic velocities. Simultaneous data from a total of 12 current meters for winter and 15 current meters for summer where incorporated into the matrix. The location with the largest directly measured internal tide amplitude was determined and used to normalize the eigenvector amplitudes and phases by forcing the eigenvector element, at that location, to be equal to its corresponding directly calculated amplitude and phase. In this manner, one can determine whether the entire eigenvector and hence, the statistical phase locking resembles the directly calculated internal tide velocity field. The eigenvector elements corresponding to the largest eigenvalue (mode one) are tabulated in Table 3. Most of the spectral power was accounted for by the first mode with the eigenvalue accounting for 74% of the variance during winter and 78% during summer. This is surprisingly high and indicates that the internal tide field is significantly coherent throughout the area of investigation for periods as long as two months, even during the

winter. Therefore, even if few modes survive at distances of the order of 100 km, they still appear to be phase locked. The mode one eigenvector elements are very close to the directly estimated amplitudes and phases. As was expected, when this analysis was performed for longer periods (i.e., 7 months), the first mode variance dropped to about 35%, reflecting the intermittentcy of the baroclinic field and the lack of absolute time overlapping of different moorings.

5. Comparison with model

The observed baroclinic field values were compared with the predictions of a modified version of a model by Prinsenberg and Rattray (1975). In the original model it was assumed that the internal tide was generated by a barotropic standing wave. However, this does not hold off the west coast of Vancouver island. A better approximation for the local tidal elevation is obtained assuming a superposition of a standing wave and of a wave traveling away from the coast (Flather 1988; Foreman and Walters 1990). Following a treatment similar to that of the original model, the baroclinic field is expressed as an infinite sum of vertically standing and horizontally progressive waves. For the purposes of this model, the topography is divided in two regions, the shelf region (I) with constant depth h_1, and the oceanic region (II) whose depth increases linearly to a constant value h_2. Under these assumptions, the total vertical barotropic and baroclinic displacement, at the shelf and oceanic regions, respectively, can be expressed as

$$\eta^{\mathrm{I}} = \{A_0^{\mathrm{I}}\psi_0^{\mathrm{I}} \cos k_0^{\mathrm{I}}(x + L) + B_0^{\mathrm{I}}\psi_0^{\mathrm{I}} \exp(ik_0^{\mathrm{I}}x) + \sum_{n=1}^{\infty} A_n^{\mathrm{I}}\psi_n^{\mathrm{I}} \exp(-ik_n^{\mathrm{I}}x)\} \exp(-i\omega t) \quad (11a)$$

$$\eta^{\mathrm{II}} = \{A_0^{\mathrm{II}}\psi_0^{\mathrm{II}} \cos k_0^{\mathrm{II}}(x + x_0) + B_0^{\mathrm{II}}\psi_0^{\mathrm{II}} \exp(ik_0^{\mathrm{II}}x) + \sum_{m=1}^{\infty} A_m^{\mathrm{II}}\psi_m^{\mathrm{II}} \exp(ik_m^{\mathrm{II}}x)\} \exp(-i\omega t), \quad (11b)$$

where A_0 is the amplitude of the standing part of the barotropic tide, B_0 is the amplitude of the progressive part of the barotropic tide, while A_n and A_m are the amplitudes of the internal wave modes. The quantity L represents the width of the shelf, and x_0 is introduced to match the phases along the boundary of the two regions. Consequently, the cross-shore component of the velocity for the shelf and oceanic regions is given by

$$u^{\mathrm{I}} = \left\{-iA_0^{\mathrm{I}} \frac{\omega}{k_0^{\mathrm{I}}} \left(\frac{\partial\psi_0^{\mathrm{I}}}{\partial z}\right) \sin\{k_0^{\mathrm{I}}(x + L)\}\psi - B_0^{\mathrm{I}} \frac{\omega}{k_0^{\mathrm{I}}} \left(\frac{\partial\psi_0^{\mathrm{I}}}{\partial z}\right) \exp(ik_0^{\mathrm{I}}x) + \sum_{n=1}^{\infty} A_n^{\mathrm{I}} \frac{\omega}{k_n^{\mathrm{I}}} \left(\frac{\partial\psi_n^{\mathrm{I}}}{\partial z}\right) \exp(-ik_n^{\mathrm{I}}x)\right\} \times \exp(-i\omega t) \quad (12a)$$

$$u^{\mathrm{II}} = \left\{-iA_0^{\mathrm{II}} \frac{\omega}{k_0^{\mathrm{II}}} \left(\frac{\partial\psi_0^{\mathrm{II}}}{\partial z}\right) \sin\{k_0^{\mathrm{II}}(x + x_0)\}\psi - B_0^{\mathrm{II}} \frac{\omega}{k_0^{\mathrm{II}}} \left(\frac{\partial\psi_0^{\mathrm{II}}}{\partial z}\right) \exp(ik_0^{\mathrm{II}}x) - \sum_{m=1}^{\infty} A_m^{\mathrm{II}} \frac{\omega}{k_m^{\mathrm{II}}} \left(\frac{\partial\psi_m^{\mathrm{II}}}{\partial z}\right) \exp(ik_m^{\mathrm{II}}x)\right\} \times \exp(-i\omega t). \quad (12b)$$

The barotropic amplitudes A_0 and B_0 were evaluated using the model of Flather. The baroclinic wavenumbers k_n, k_m and vertical eigenfunctions ψ_n, ψ_m were obtained by numerically solving Eq. (4). By matching the motion along the boundary of the shelf and oceanic regions, the baroclinic amplitudes A_n, A_m, can be estimated:

$$\sum_n A_n^{\mathrm{I}} P_{rm}^{\mathrm{I}} = A_0^{\mathrm{I}} \cos(k_0^{\mathrm{I}}L) S_r^{\mathrm{I}} + B_0^{\mathrm{I}} T_r^{\mathrm{I}} + \sum_m A_m^{\mathrm{II}} Q_{rm}^{\mathrm{II}}, \quad r = 1, n \quad (13a)$$

$$\sum_m A_m^{\mathrm{II}} P_{jm}^{\mathrm{II}} = A_0^{\mathrm{II}} \cos(k_0^{\mathrm{II}}x_0) S_j^{\mathrm{II}} + B_0^{\mathrm{II}} T_j^{\mathrm{II}} + \sum_n A_n^{\mathrm{I}} Q_n^{\mathrm{I}}, \quad j = 1, m. \quad (13b)$$

The coefficients S, T, Q, P are defined in the Appendix.

The model was evaluated for mooring E03 where the topography resembles that of the model, and the internal tide signal was found to be the strongest. A total of $m = 40$ modes for the oceanic region and $n = 8$ modes for the shelf region were implemented in the computation. The procedure was performed for two seasons, winter and summer. The model results were compared with the experimental values that were obtained from the EOF analysis (Table 3) and are plotted in Fig. 10 and Fig. 11. Along with the revised model predictions, the original model results are also plotted. During winter, ten modes were enough to describe the amplitude. However, there is about 70° (2 h) phase difference between model and observations. During summer, all 40 modes were superimposed in the output of the model. Here, due to the fact that the internal tide signal is much stronger, the agreement between model and observations is remarkably good. It is also evident that the disagreement found by Barbee et al. (1975), that is, small model amplitudes and 180° phase difference, is settled with the introduction of the traveling wave term.

TABLE 3. Properties of the eigenvector corresponding to the largest eigenvalue. The amplitudes (u and v) have dimensions in centimeters per second, and the corresponding phases are in degrees. The quantity δ_r represents the variance accounted for by this eigenmode.

Mooring	Depth (m)	u (cm s^{-1})	g_u (deg)	v (cm s^{-1})	g_v (deg)	δ_r (%)
			Winter			
E01	85	1.1	157	2.0	353	
E02	110	1.2	317	0.9	196	
E03	350	1.7	253	2.4	154	
	550	2.8	192	2.4	123	
	750	2.4	139	1.5	31	
E04	350	0.8	280	2.3	176	74
	550	1.3	292	1.8	177	
	750	0.8	339	1.1	174	
	1000	1.6	170	1.3	92	
	1250	2.9	179	2.2	90	
E05	50	4.5	268	4.3	180	
	500	0.3	267	0.7	159	
			Summer			
E01	50	1.0	54	1.8	1	
	85	5.2	154	6.5	60	
E02	50	4.6	229	5.1	128	
	110	1.3	84	1.1	141	
E03	60	3.9	81	5.6	335	
	350	3.0	336	3.6	231	
	550	0.7	292	1.7	218	78
	750	6.1	174	5.5	77	
E04	50	9.8	29	8.8	296	
	350	2.5	265	3.3	167	
	550	1.5	335	1.9	221	
	1000	1.9	60	1.4	333	
	1250	1.5	124	1.4	25	
E05	1000	1.8	155	1.7	72	
E2B	60	3.3	172	6.3	48	

6. Internal tide–eddy interaction

From late July to early September (days 570–610), a cyclonic eddy was observed over the continental margin between Brooks Peninsula and Estevan Point, near section E. During summer, the mean surface flow reversed direction southward following a changing wind pattern, and early in August the northward California Undercurrent reached section E. The strong vertical shear present in August resulted in a mean flow conducive to baroclinic instability, which in turn provided a meander with energy to evolve into a mesoscale eddy (Thomson 1984).

The evolution of the internal tide coefficients near the eddy formation area (e.g., Figs. 6, 7) revealed the following (note that vertical lines demarcate the period during which the eddy was observed in the region). At the beginning of June, around day 520, the internal tide field gained strength. This reflects the seasonal evolution of the water column toward higher stratification as shown in Fig. 8. The buildup continued until the beginning of July when the internal tide leveled off. Toward the end of the month its amplitude decreased until the beginning of September. The internal tide attenuation coincided with the formation of the eddy in the region (days 570–610). Possible causes are

(i) a steepening of the isopycnals caused a modification of the ray path and thus a decrease in the internal tide strength at particular stations;

(ii) the internal tide reached its peak and started breaking (self-destruction);

(iii) the eddy modified the density field at the generation region and a smaller internal tide was generated; and

(iv) the eddy pumped energy from the internal wave field.

In order to investigate the validity of cause a, rays were traced before and after the eddy activity, taking into account changes in density gradients. The outcome produced almost identical ray paths before and after the event, and therefore, the possibility was rejected. For b to be valid, that is, for internal tidal mixing to occur, the Richardson number should be less than 0.25 (e.g., New 1988):

$$\mathrm{Ri} \approx \left[0.8 \frac{N}{\partial u/\partial z}\right]^2 < 0.25, \qquad (14)$$

where u is the cross-shore component of the velocity and the factor 0.8 reflects the relationship between u and v. However, after evaluating Eq. (14) for the time interval under investigation near the generation region, it was found that Ri was always above the critical value (0.25), and possibility b was rejected. Option c can be verified by observing the density field near the generation region. The shape of the isopycnals in the area during the July (not shown) and September (Fig. 8b) cruises reveals a shoaling of the pycnocline during September, possibly due to the radiation field from the eddy over the slope tilting the isopycnals upward at the shelf break. This displaced the location of $N_{\max}$ (interface) closer to the surface and away from the generation region, thereby weakening the internal tide driving force. It is evident from the harmonic analysis that attenuation also occurred at depth, such as at E03 750 m (Fig. 6b), where the density field remained practically constant all year. Furthermore, the coherence of this record and that of E04 50 m was found to be extremely high (coherence 0.9). This leads to the conclusion that the internal tide behavior during the eddy period is dictated not by localized variations but due to modifications of the pycnocline near the generation region (where the body force is proportional to N^2). Finally, for option d to hold, one would have to show a significant correlation between the uv Reynolds stress and the production of eddy kinetic energy. One eddy event does not produce enough data to verify option d.

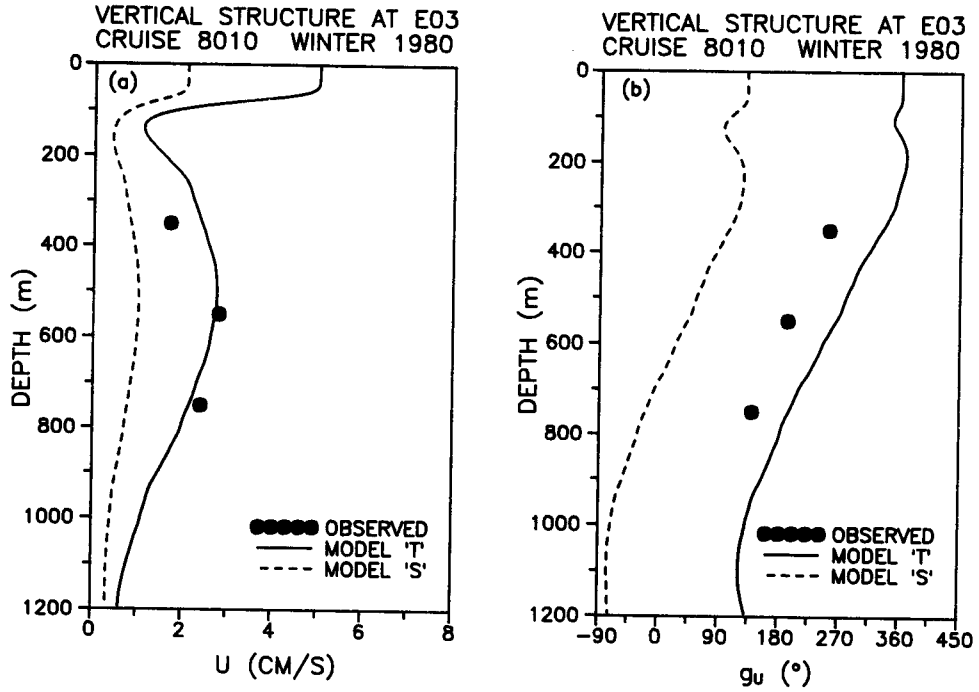

FIG. 10. Profiles of cross-shore velocity; (a) amplitude and (b) phase for mooring E03 during winter 1980. Circles denote field values resulted from the EOF analysis. Dashed lines are the predictions of the model by Prinsenberg and Rattray (1975), referred to here as model "S." In this model the barotropic wave is expressed by a standing wave. Solid lines are predictions of its modified version, referred to here as model "T." In this version, the barotropic wave is modeled by a superposition of a standing wave and a traveling wave. The sum of ten output oceanic modes is displayed.

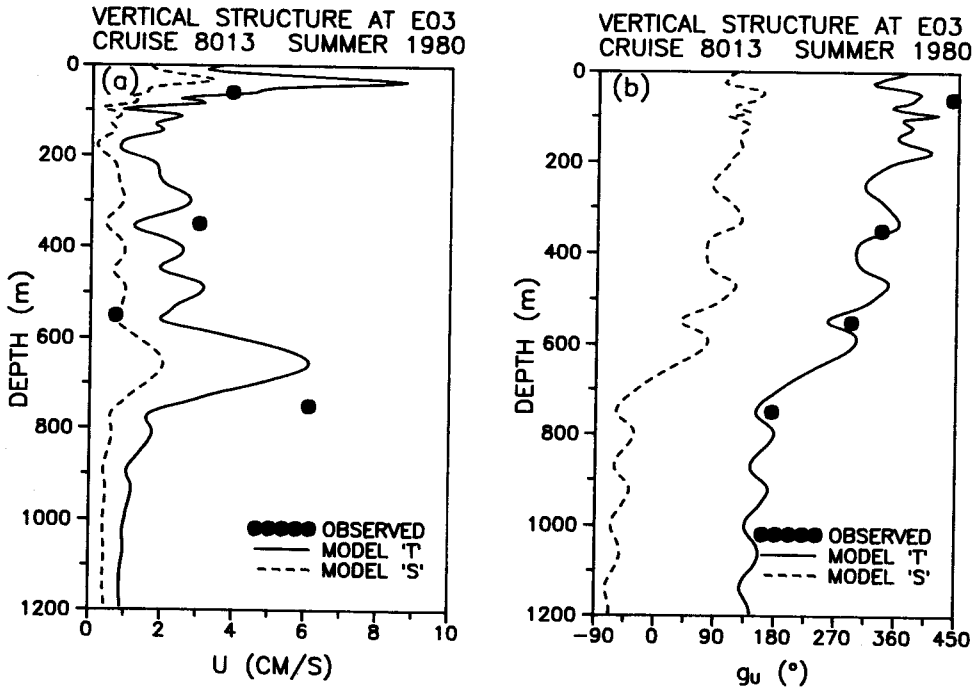

FIG. 11. Same as in Fig. 10 but for summer conditions; the output oceanic modes are 40.

7. Conclusions

Although the semidiurnal barotropic tidal current is weak near the west coast of Vancouver Island, when it interacts with the density structure and the supercritical continental slopes of the area, it can force a large baroclinic field. The baroclinic field is highly intermittent and follows the seasonal development of the density stratification (weak during winter, strong during summer). The direction of propagation was generally perpendicular to the isobaths and offshore away from the shelf break. At least for one location (E section), where the bottom bathymetry was relatively regular and a large amount of field data existed, a downward propagating beam and a weaker upward beam, both emanating from the shelf break, were observed 40 km away from the generation region. The downward beam was found to follow the slope of characteristics according to the expected seasonal pattern. The baroclinic field on the shelf, although strong, was very noisy, and a beam pattern was not established. An eigenvector analysis performed for the area of section E revealed high spatial coherence both for winter and summer. Comparison of the observations with a modified version of a model by Prinsenberg and Rattray (1975) gave a good agreement, particularly for the summer season. Internal tide generation models are sensitive to the form of barotropic forcing. The failure of a previous intercomparison (Barbee et al. 1975) was explained with the introduction of a small traveling wave term in the expression for the barotropic tide. A cyclonic eddy present in the area during August 1980 interfered with the internal tide and reversed its growth. It is suggested that the radiation field from the eddy modified the density structure near the generation region resulting in weaker internal tide forcing.

Acknowledgments. We wish to acknowledge H. J. Freeland, R. E. Thomson, and W. R. Crawford for making the data available to us; M. G. G. Foreman for providing the tidal analysis program and the results of his numerical model; and M. Stacey for helpful discussions. This work was financed through a DND/NSERC fellowship and the ARP program RR15.

APPENDIX

Definition of Model Coefficients

The coefficients S, T, Q, P are defined as follows:

$$S_r^{\mathrm{I}} = \int_0^{h1} \left\{ \psi_0^{\mathrm{II}} \left[\cos\left(k_0^{\mathrm{II}} \frac{z}{\alpha}\right) - \frac{k_0^{\mathrm{II}}}{k_0^{\mathrm{I}}} \tan(k_0^{\mathrm{I}} L) \sin\left(k_0^{\mathrm{II}} \frac{z}{\alpha}\right) \right] + \psi_0^{\mathrm{I}} \left[\sin\left(k_0^{\mathrm{I}} \frac{z}{\alpha}\right) \tan(k_0^{\mathrm{I}} L) - \cos\left(k_0^{\mathrm{I}} \frac{z}{\alpha}\right) \right] \right\} \times (N^2 - \omega^2) \exp\left(ik_r^{\mathrm{I}} \frac{z}{\alpha}\right) \psi_r^{\mathrm{I}} dz \quad \text{(A1)}$$

$$S_j^{\mathrm{II}} = \int_0^{h2} \left(-\frac{\psi_0^{\mathrm{II}}}{k_0^{\mathrm{II}}}\right) \left[\sin\left(k_0^{\mathrm{II}} \frac{z}{\alpha}\right) + \frac{k_0^{\mathrm{II}}}{k_0^{\mathrm{I}}} \tan(k_0^{\mathrm{I}} L) \cos\left(k_0^{\mathrm{II}} \frac{z}{\alpha}\right) \right] (N^2 - \omega^2) \exp\left(ik_j^{\mathrm{II}} \frac{z}{\alpha}\right) \psi_j^{\mathrm{II}} dz + \int_0^{h1} \left(-\frac{\psi_0^{\mathrm{I}}}{k_0^{\mathrm{I}}}\right) \left[\sin\left(k_0^{\mathrm{I}} \frac{z}{\alpha}\right) + \tan(k_0^{\mathrm{I}} L) \cos\left(k_0^{\mathrm{I}} \frac{z}{\alpha}\right) \right] (N^2 - \omega^2) \exp\left(ik_j^{\mathrm{II}} \frac{z}{\alpha}\right) \psi_j^{\mathrm{II}} dz \quad \text{(A2)}$$

$$T_r^{\mathrm{I}} = \int_0^{h1} \left\{ \psi_0^{\mathrm{II}} \left[\left(1 - \frac{k_0^{\mathrm{II}}}{k_0^{\mathrm{I}}}\right) \cos\left(k_0^{\mathrm{II}} \frac{z}{\alpha}\right) + \frac{k_0^{\mathrm{II}}}{k_0^{\mathrm{I}}} \exp\left(k_0^{\mathrm{II}} \frac{z}{\alpha}\right) \right] - \psi_0^{\mathrm{I}} \exp\left(ik_0^{\mathrm{I}} \frac{z}{\alpha}\right) \right\} (N^2 - \omega^2) \exp\left(ik_r^{\mathrm{I}} \frac{z}{\alpha}\right) \psi_r^{\mathrm{I}} dz \quad \text{(A3)}$$

$$T_j^{\mathrm{II}} = \int_0^{h2} \frac{\psi_0^{\mathrm{II}}}{k_0^{\mathrm{II}}} \left[\left(\frac{k_0^{\mathrm{II}}}{k_0^{\mathrm{II}}} - 1\right) \sin\left(k_0^{\mathrm{II}} \frac{z}{\alpha}\right) - \frac{\psi_0^{\mathrm{II}}}{ik_0^{\mathrm{I}}} \exp\left(ik_0^{\mathrm{II}} \frac{z}{\alpha}\right) \right] (N^2 - \omega^2) \exp\left(-ik_j^{\mathrm{II}} \frac{z}{\alpha}\right) \psi_j^{\mathrm{II}} dz + \int_0^{h1} \frac{\psi_0^{\mathrm{I}}}{ik_0^{\mathrm{I}}} \exp\left(ik_0^{\mathrm{I}} \frac{z}{\alpha}\right) (N^2 - \omega^2) \exp\left(-ik_j^{\mathrm{II}} \frac{z}{\alpha}\right) \psi_j^{\mathrm{II}} dz \quad \text{(A4)}$$

$$Q_{jn}^{\mathrm{I}} = \int_0^{h1} \frac{i}{k_n^{\mathrm{I}}} \exp\left\{-i(k_n^{\mathrm{I}} + k_j^{\mathrm{II}}) \frac{z}{\alpha}\right\} (N^2 - \omega^2) \psi_j^{\mathrm{II}} dz \quad \text{(A5)}$$

$$Q_{rm}^{\mathrm{II}} = \int_0^{h1} \exp\left\{i(k_r^{\mathrm{I}} + k_m^{\mathrm{II}}) \frac{z}{\alpha}\right\} (N^2 - \omega^2) \psi_m^{\mathrm{II}} \psi_r^{\mathrm{I}} dz \quad \text{(A6)}$$

$$P_{rm}^{\mathrm{I}} = \int_0^{h1} \exp\left\{-i(k_n^{\mathrm{I}} - k_r^{\mathrm{I}}) \frac{z}{\alpha}\right\} (N^2 - \omega^2) \psi_n^{\mathrm{I}} \psi_r^{\mathrm{I}} dz, \quad \text{(A6)}$$

$$r \neq n \quad \text{(A7a)}$$

$$P_{rn}^{\mathrm{I}} = g, \quad r = n \quad \text{(A7b)}$$

$$P^{II}_{jm} = \int_0^{h2} \frac{1}{ik^{II}_m} \exp\left\{ i(k^{II}_m - k^{II}_j)\frac{z}{\alpha} \right\} \times (N^2 - \omega^2)\psi^{II}_m \psi^{II}_j dz, \quad m \neq j \quad \text{(A8a)}$$

$$P^{II}_{jm} = \frac{g}{ik^{II}_m}, \quad m = j. \quad \text{(A8b)}$$

Here h_1 and h_2 are the shelf and oceanic depths, respectively (positive downward), and α is the bottom slope along the boundary.

REFERENCES

Baines, P. G., 1974: The generation of internal tides over steep continental slopes. *Phil. Trans. Roy. Soc. London,* **227,** 27–58.

Barbee, W. B., J. G. Dworski, J. D. Irish, L. H. Larsen, and M. Rattray, Jr., 1975: Measurement of internal waves of tidal frequency near a continental boundary. *J. Geophys. Res.,* **80,** 1965–1974.

Crawford, W. R., and R. E. Thomson, 1982: Continental shelf waves of diurnal period along Vancouver Island. *J. Geophys. Res.,* **87,** 9516–9522.

Flather, R. A., 1988: A numerical model investigation of tides and diurnal-period continental shelf waves along Vancouver Island. *J. Phys. Oceanogr.,* **18,** 115–139.

Foreman, M. G. G., 1978: Manual for tidal currents analysis and prediction. Pacific Marine Science Report No. 78-6. Institute of Ocean Sciences, Sidney, 70 pp.

——, and R. A. Walters, 1990: Finite elements tidal model for the southwest coast of Vancouver Island. *Atmos.-Ocean.* **28,** 261–287.

Groves, G. W., and E. J. Hannon, 1968: Time series regression of sea level on weather. *Rev. Geophys.,* **6,** 129–174.

Huggett, W. S., W. R. Crawford, R. E. Thomson, M. V. Woodward, 1987: Data record of current observations, Vol. XIX, Institute of Ocean Sciences, Sidney.

Huthnance, J. M., and P. G. Baines, 1982: Tidal currents in the northwest African upwelling region. *Deep-Sea Res.,* **29,** 285–306.

Kundu, P. K., R. E. Thomson, B. M. Hickey, and P. H. LeBlond, 1988: Interaction of internal waves and mean flow observed near a coast. *J. Mar. Res.,* **46,** 1–23.

Larsen, L. H., M. Rattray, Jr., W. B. Barbee, and J. G. Dworski, 1972: Internal tides. *Rapp. Proc. V. Reun.,* **162,** 65–79.

Levine, M. D., and J. G. Richman, 1989: Extracting the internal tide from data: Methods and observations from the Mixed-Layer Dynamics Experiment. *J. Geophys. Res.,* **94,** 8125–8134.

Marsden, R. F., 1986: The internal tide on Georges Bank. *J. Mar. Res.,* **44,** 35–50.

Mooers, C. N. K., 1973: Several effects of a baroclinic current on the cross-stream propagation of inertial-internal waves. *Geophys. Fluid Dyn.,* **6,** 245–275.

New, A. L., 1988: Internal tidal mixing in the Bay of Biscay. *Deep-Sea Res.,* **35,** 691–709.

Pingree, R. D., and A. L. New, 1989: Downward propagation of internal tidal energy into the Bay of Biscay. *Deep-Sea Res.,* **36,** 735–738.

——, ——, 1991: Abyssal penetration and bottom reflection of internal tidal energy in the Bay of Biscay. *J. Phys. Oceanogr.,* **21,** 28–39.

Prinsenberg, S. J., and Maurice Rattray, Jr., 1975: Effects of continental slope and variable Brunt–Vaisala frequency on the coastal generation of internal tides. *Deep-Sea Res.,* **22,** 251–263.

Thomson, R. E., 1984: A cyclonic eddy over the continental margin of Vancouver island: Evidence for baroclinic instability. *J. Phys. Oceanogr.,* **14,** 1326–1348.

——, and W. R. Crawford, 1982: The generation of diurnal period shelf waves by tidal currents. *J. Phys. Oceanogr.,* **12,** 635–643.

Wunsch, Carl, 1975: Internal tides in the ocean. *Rev. Geophys.,* **13,** 167–182.